Application of Hot Powder Bed Compaction in Additive and Subtractive Composite Manufacturing Demonstrating Improved Performance and Flexible Fusion.

Jimesh D. Bhagatji[a]*, Theodore Osuniga[a], Gonzalo Fernandez[a], Oleksandr G. Kravchenko[a]
[a] Department of Mechanical Engineering, Old Dominion University, Norfolk, VA 23529, US
* *Corresponding author (jbhag001@odu.edu)*

Keywords: Additive Manufacturing, Lattice Sandwich Structure, Thermoplastic Composites, Isostatic Compaction, , Material Characterization

Abstract

Material Extrusion (MEX) enables the additive manufacturing of fiber-reinforced thermoplastic composites with tailored fiber orientations for optimized performance. However, MEX-processed parts suffer from defects such as micro-voids, weak interlayer fusion, and poor fiber-matrix interfaces, limiting their mechanical reliability. This study explores Hot Powder Bed Compaction (HPBC), a flexible fusion process that applies isostatic compaction without rigid tooling, significantly enhancing the structural integrity of MEX composites. HPBC-treated components—including topological rocker and 2D-lattice sandwich structures—exhibited notable property enhancements while maintaining intricate geometries. Coupled-level characterization demonstrated a 30.2% increase in flexural modulus (14.9 GPa) and a 20.8% increase in tensile modulus (31.1 GPa), while flexural strength (360 MPa) and tensile strength (285 MPa) improved by 36.4% and 61.9%, respectively. Moreover, the topological rocker component exhibited a 31.3% increase in stiffness compared to the pristine MEX component. HPBC-treated sandwich structure showed significant structural improvements, with a 119% increase in stiffness per unit width (235.5 N/mm²) and a 154.3% improvement in strength (753.0 N/mm). These enhancements were attributed to improved interlayer fusion, crack healing, and inter- and intra-void closure, as observed through microscopy and fracture surface analysis. This study demonstrates HPBC's potential for fabricating high-performance, complex-shaped, and tunable composite structures, particularly for applications requiring resilience under repeated loading.

1. Introduction

The increasing adoption of continuous fiber-reinforced thermoplastic composites [1, 2] in

industries prioritizing high-performance and lightweight solutions, particularly in the automotive [3] and aerospace [4, 5] sectors, demonstrates a growing demand for advanced thermoplastic fabrication methods. This increase in the use of thermoplastic composites is attributed to several advantages over traditional thermosetting composites, including superior impact resistance [6], fracture resistance [7], repairability [8] [9], and recyclability [10]. The integration of high-performance thermoplastics with topological shape optimization and sandwich structure with the continuous fiber alignment [11] can further enhance strength, reduce weight [12], and optimize material utilization. The use of composite corrugated core [13] or truss-core sandwich panels, characterized by continuous fiber alignment along the truss direction, is increasing due to its superior resistance to bending loads [14, 15] by providing high shear stiffness [16–18] compared to traditional foam, honeycomb, and lattice core sandwich panels. However, manufacturing complex architectures [19–21] poses significant challenges with conventional manufacturing techniques.

Conventionally, fiber-reinforced thermoplastic components rely on injection or compression molding (shown in Fig.1) [22] to achieve 3D shapes, which necessitates molds that limit the geometrical complexity of the molded parts. Furthermore, injection molded parts are limited by the short fiber length due to an increase in viscosity [23], which, in turn, is limited by the injection pressure. By combining thermo-stamping of continuous or long discontinuous fiber-reinforced thermoplastic (FRP) laminates [24] with overmolded short-fiber-reinforced plastics [25] allows for high-performance structures [26]. However, in any molding process specialized tooling is needed, requiring significant investment and time and cost, which may be prohibitively expensive. Similarly, traditional sandwich manufacturing methods [27] for lattice truss-core structures often require molds with intricate geometries, leading to labor-intensive and costly processes. These methods typically involve multiple steps, including the separate curing of core and skin materials followed by adhesive bonding, which not only increases production time and cost but also limits the ability to realize variable or topology-optimized core designs. Consequently, for ease of fabrication, foam or honeycomb sandwich composites are often preferred. However, such conventional cores offer limited geometric flexibility, as they are constrained to standard shapes and sizes, restricting their ability to be tuned for specific load paths, performance requirements, or multifunctional roles.

Additive manufacturing (AM), such as material extrusion process can address these limitations while offering another advantage of controlled fiber orientation deposition. However, the mechanical properties of MEX composites part suffer from previously mentioned manufacturing induced defects and locked-in residual stresses [28, 29]. To address these issues different post-treatment techniques have been proposed, which can involve annealing or hot temperature compaction [30–32] of FRP parts. Nonetheless, there is still a need for improving the mechanical performance of MEX parts by removing the associated MEX induced defects especially for complex geometries.

The recently developed flexible fusion process is proposed to address this limitation by using hot powder bed compaction (HPBC) technique [33] to achieve reconsolidation of MEX processed components. HPBC is a process of creating hydrostatic stresses, characterized by the non-linear, time-dependent compaction behavior of molten FRP and of the consolidated powder bed itself that is used to support the structural component during the fusion process. HPBC takes inspiration from the widely adopted hot isostatic pressing (HIP) [27], which has been used to improve the mechanical properties of metallic components producing by casting or AM and more recently FRP [36] by providing for full densification during the subsequent application of heat and pressure inside of the hermetic chamber. Many of the same benefits found in HIP can be seen in HPBC; however, HPBC differs from HIP by not relying on compressed gasses, instead controlling the hydrostatic stresses via the degree of powder compaction. Therefore, the use of powder creates a new level of interaction between the part and the densified medium, both of which influence the final geometry and material properties. As a result, HPBC allows to ease the requirement on the processing technology compared to the HIP process, such that a generic tool cavity can be used without a need for pressure vessel used in HIP. However, there are other substantive differences from the material point of view, HPBC utilizes complete or partial melting of the treated component to accelerate and improve fusion bonding between the internal material interfaces, like cracks and voids, which are left during AM process.

The HPBC is demonstrated on both additively and subtractively manufactured components. This includes complex topological parts and sandwich structures produced via additive

manufacturing, as well as a hinge bracket fabricated from water-jet cut glass fiber-reinforced polymer (FRP) laminates using subtractive methods. This study demonstrated HPBC's ability to close the voids and cracks in complex 3D-printed parts and standard laminated assembly, highlighting its effectiveness for intricate geometries and multi-material systems. HPBC involves the following consecutive steps. The first step of powder densification process was analyzed with Dynamic Mechanical Analysis (DMA) using uniaxial compaction and stress relaxation to understand the non-linear, time-dependent powder compaction mechanics. During the powder compaction, powder displacement and densification occurs around the MEX part in the intricate open pockets of the component. The next step of the HPBC treatment, the consolidation process during which heat and isostatic pressure are applied. This step is essential for eliminating macro voids that are challenging to remove even through annealing [25].

Combined with the advantage of the flexibility of additive manufacturing in creating 3D structures and without a need for specialized tooling, HPBC was demonstrated to improve mechanical properties of MEX material and of the topological rocker, which was designed based on multi-load cases. The design, print layer sequence, HPBC processing parameters and dimensional stability for the rocker component are discussed in the section-2. The section-3 delves into the characterization of the HPBC process and its impact on material properties, particularly on the understanding the powder compaction mechanics, which is essential for selecting the appropriate isostatic pressure. Characterization of uniaxial powder compaction was proposed based on dynamic mechanical analyzer (DMA) setup, which was later used for selecting isostatic pressure for composite consolidation using HPBC. A comprehensive material characterization post HPBC included differential scanning calorimetry (DSC), microscopy, and mechanical testing through flexural and tensile testing. The final section provides a discussion regarding the interlaminar fusion, degree of crystallinity post HPBC, along with flexural performance of specimen, and mechanical behavior of the rocker under tensile load. Together, these assessments provide a detailed understanding of the HPBC process and its influence on the mechanical performance of the FRP MEX composites.

2. Hot Powder Bed Compaction

Materials and test coupons

The specimens were 3D printed using the dual-nozzle Markforged Mark Two printer. One nozzle was used for printing short, discontinuous carbon fibers (SCF) filament, while the other nozzle was used for depositing long discontinuous carbon fibers (LCF) filament. Both material systems were procured from Markforged. The SCF is micro carbon fiber reinforced PA6 [37] with a 10.5% fiber volume fraction [30, 38], while LCF is continuous carbon fiber with a 45% fiber volume fraction [38]. These fiber volume fractions were calculated using Thermogravimetric Analysis (TGA) [30, 38], which provides the weight fractions. The volume fraction was then obtained using the filament density from the Markforged datasheet. Markforged Eiger software served as the slicer for the layer's configuration of LCF and SCF, with a 0.125 mm layer thickness in the specimen.

The layer sequence comprised of one layer of LCF sandwiched between two layers of SCF. In this configuration, the adjacent SCF layers were aligned at [+45°/-45°] relative to the X-axis, resulting in a balanced layer orientation. Based on the LCF layer, two types of test coupons—flexural coupons and tensile dogbone coupons —were printed with fiber orientations of 0° and 90°. Both flexural and tensile coupons consisted of 14 LCF layers and 16 LCF layers, respectively, following the discussed layer configuration. Additionally, four layers of SCF were included on both the top and bottom of the coupon to stabilize the LCF layers. All the layers were printed with 100% infill and a wall thickness of two layers to ensure layers integrity and surface quality. The printing head temperatures were set to 265°C for the SCF filament and 270°C for the LCF filament, with deposition rates of 20 mm/s and 15 mm/s, respectively, on an unheated print bed. This layer configuration and print parameters were kept consistent across tensile and flexural specimens, and the rocker, with the only variation being the orientation of the LCF. For HPBC process, a 10-micron talc powder was used supplied from Fasco Epoxies [39]. The resulting overall fiber volume fraction of 17.78% was determined for both LCF and SCF printed layers.

HPBC consolidation process

The HPBC process consists of three steps performed using general-purpose mold: (I) Initial powder densification; (II) Heating; (III) Consolidation of MEX part during cool-down.

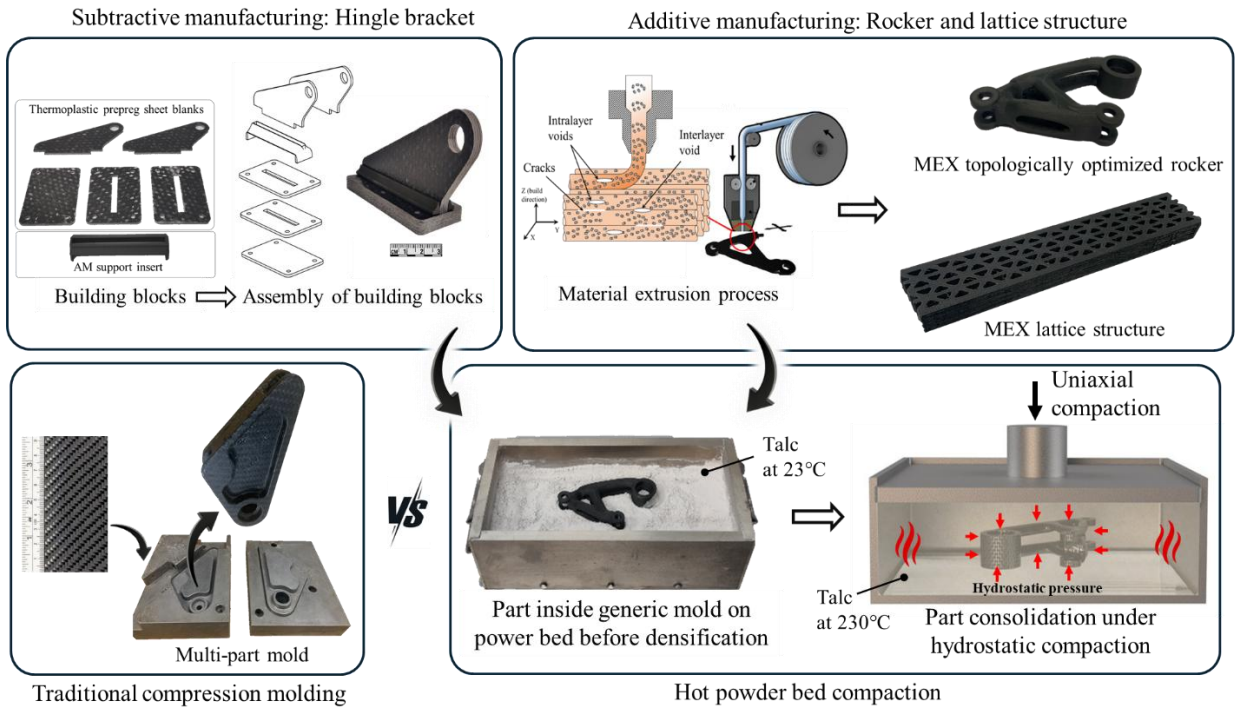

Figure. 1: The Process flow for HPBC from inter and intra-layer defects during MEX process, placement of rocker on talc bed and three-step HPBC.

A smaller mold measuring 125 x 125 mm^2 with a 25 mm height was used for HPBC of flexural and tensile specimens, while a larger mold measuring (shown in Fig. 1) 125 x 250 mm^2 with a 100 mm height was used for the rocker, bracket and sandwich structure. The parts are used for the HPBC, are different in shape and size with complete geometric features made from additively manufactured and subtractively manufactured but still consolidated in single mode. Initially, the part was immersed in a talc bed within a mold (Fig. 1) and subjected to room temperature densification in a Wabash hydraulic hot press. Fine powder medium, such as talc [39], plays an important role of providing a flexible medium during HPBC, which can be densified to conform to the complex part geometry. For specimens, a 1-ton compaction load was applied, while the rocker was subjected to about 2-ton load, each for 10 minutes during densification and consolidation stage. The load was determined to ensure a compaction pressure of 500 kPa through densified talc. During the heating stage, the mold was heated to reach the melting temperature of PA6 at 230°C inside a Carbolite laboratory convection oven. The smaller mold was kept inside the oven for 90 minutes to reach the desired temperature, while the larger mold intended for the rocker required 180 minutes to attain the target temperature. The mold temperature was monitored via the thermocouple and IR thermometer. The final stage of isostatic consolidation was accomplished

during the cooldown process under the applied compressive force (illustrated in Fig. 1). The load and duration remained consistent for talc densification and MEX part consolidation stages. At the end of the heating stage, the matrix within the LCF and SCF was fully melted, and the compaction force closes the macro-void resulting in improved consolidation of the MEX printed part. After reaching room temperature, the part, covered with talc, was taken out of the mold (Fig. 2a.) and sandblasted to remove the talc from the surface (Fig. 2a). The fused talc on surface was removed via sandblasting with a 60 US mesh abrasive, resulting in a smooth surface finish

Design of additively manufactured Rocket, lattice structure and subtractively manufactured bracket

To determine the topological geometry of a rocker a block design space was provided with two design constraints and four load cases outlined in Fig. 2a. The shape optimization analysis was performed using Altair Inspire software [40]. The shape optimization process utilized boundary condition input data for the rocker pivot point (*Pin-1*), push bar mount (*F*), and spring-damper mount (*Pin-2*) in the design space (shown in Fig. 2a), along with loading conditions corresponding to various load cases, as shown in Fig. 2a. To ensure symmetry, a shape control constraint was applied to the XY-plane. The optimization objective was to minimize mass while maintaining a minimum safety factor constraint of 2 using assigned nominal mechanical properties of the material: E = 30 GPa and n = 0.32. As a result of topology optimization, the structural element exhibited complex geometry shown in Fig. 2a with curvilinear openings in the rocker's arms. The optimized rocker underwent slicing, resulting in 156 layers, as indicated by the vertical bar in Fig. 2a. Among these, 20 layers consisted of LCF, and the rest were SCF, each with a layer height of 0.125 mm. LCF layers were placed in two symmetric arms. The continuous fiber reinforcement encircled all three mounting holes, achieved through the inside-outside wall, concentric fiber path feature in Eiger, as depicted in Fig. 2a.

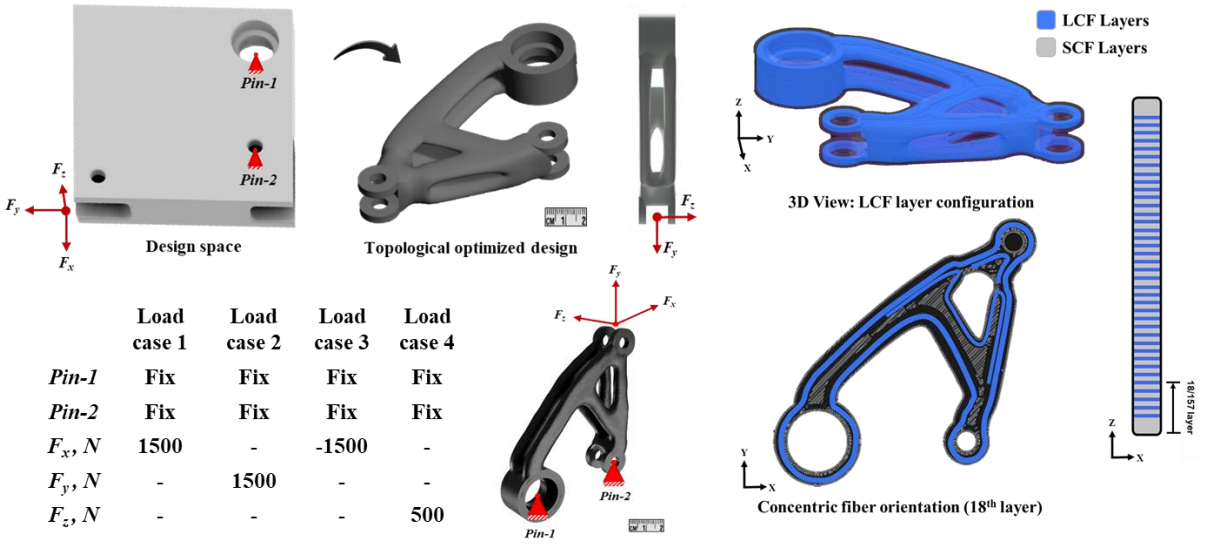

	Load case 1	Load case 2	Load case 3	Load case 4
Pin-1	Fix	Fix	Fix	Fix
Pin-2	Fix	Fix	Fix	Fix
F_x, *N*	1500	-	-1500	-
F_y, *N*	-	1500	-	-
F_z, *N*	-	-	-	500

(a)

(b)

Parametric geometry of the lattice structures

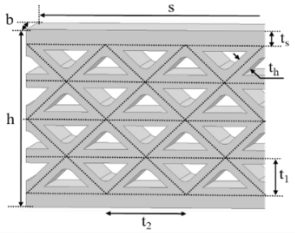

	Pristine (mm)		HPBC (mm)	
	SR4	SR2	SR4	SR2
h	28.4	28.4	28.25	29.35
b	15	15	12.28	12.36
t_1	6	12	5.92	11.89
t_2	12	24	12.21	24.37
t_h	2.2	4.4	2.75	5.63
t_s	2.2	2.2	2.19	2.19
s	144	144	146.13	146.23

Lattice coupon geometry

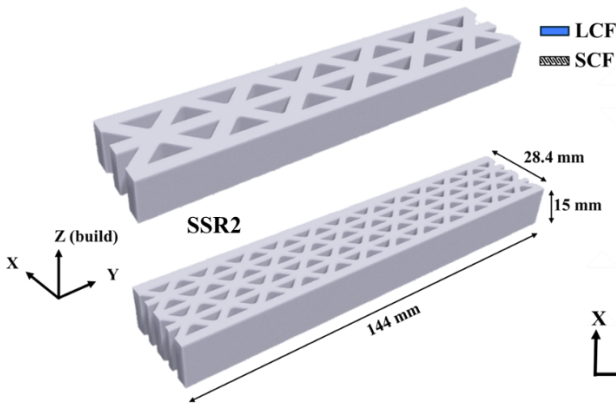

Tailored fiber orientation in truss direction

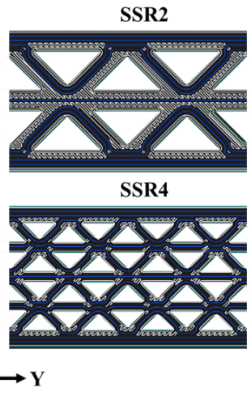

(c)

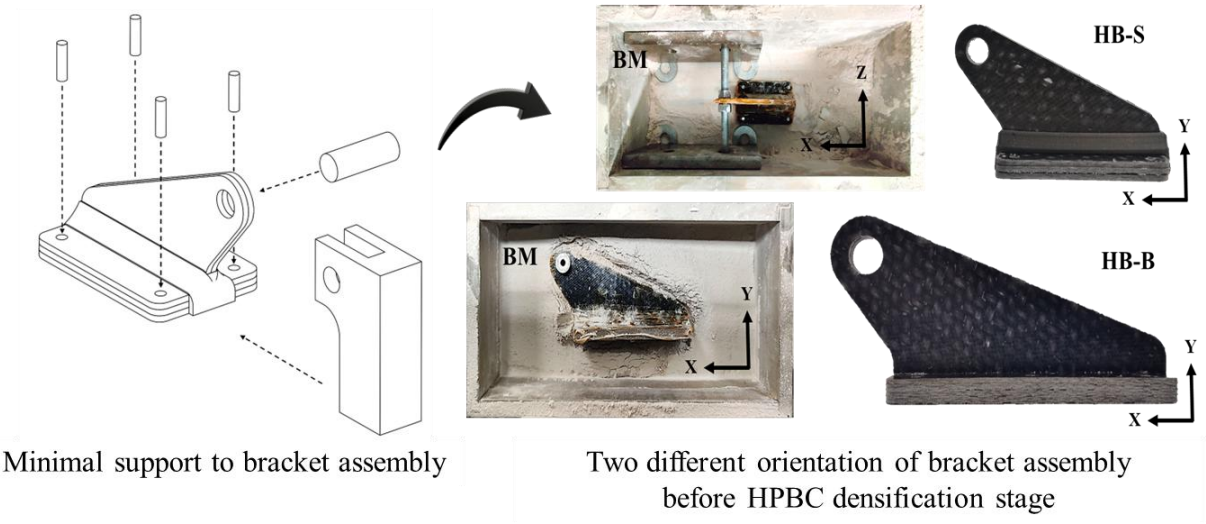

(d)

Figure 2. (a) Rocket design space used for optimization and the topological design with 73.4% volume reduction with LCF fiber layup configuration. (b) Pristine rocker, HPBC-treated rocker (covered with talc), and treated rocker after sandblasting. (c) Truss-core sandwich structure design with R4 and R2 configuration with dimension of pristine and post-HPBC treatment along tailored truss-oriented LCF (d) Different orientation used of hinge bracket for HPBC treatment.

To study the effect of core geometry on flexural performance, two triangular truss-based core designs were developed (shown in Fig. 2b), chosen for their superior shear resistance in lightweight structures. Both designs maintained a constant relative density of 0.7 g/cm³ by varying the unit cell size and number of core rows: a four-row core (R4) with 2.2 mm trusses and a two-row core (R2) with 4.4 mm trusses. This allowed evaluation of damage tolerance under bending while keeping overall beam height and truss geometry constant. LCF-reinforced skins were co-printed with the truss core – to avoid secondary bonding – using a Markforged Mark Two printer. To maintain uniform fiber reinforcement in LCF layer, a single LCF tow was embedded in each truss of the R4 core, whereas two LCF tows were used per truss in the R2 core to match the total fiber volume (shown in Fig. 2b). Additionally, both configurations included two LCF tows in the top and bottom skins. This consistent reinforcement strategy ensured that any differences in mechanical response could be attributed primarily to core geometry rather than variations in fiber content.

The hinge bracket was fabricated through the assembly of vertical and horizontal blanks (shown in Fig.1). These blanks are interconnected using a tongue-and-groove joint, in which the vertical blank possesses a tongue while the horizontal blank features a corresponding groove. The

vertical blank comprises a stack of two identical profiles prepreg sheets. On the other hand, the horizontal blank consists of three prepreg sheets, with two of them featuring grooves, while the bottom without groove, as depicted in Fig. 1. To secure these blanks assembly in place, MEX with SCF, was used as fillet-shaped support insert. Lastly, the entire assembly was secured by taping all of its edges with polyimide tape. Two different sizes of hinge brackets—referred to as the small hinge bracket (HB-S) and the big hinge bracket (HB-B)—were designed and compacted using different orientations during the HPBC process. The HB-S was positioned vertically in the powder bed with minimal support to maintain the upright orientation of its vertical flange (as shown in Fig. 2c), while the HB-B was placed horizontally in the powder bed without any metal support.

3. Experimental Characterization

Characterization of isostatic powder bed compaction using DMA

The characterization of talc bed densification was performed using a closed-die uniaxial compaction test conducted with DMA from Anton Paar (MCR 702e MultiDrive) [41] (Fig. 3a). To accommodate the experimental setup, a custom 3-piece small mold (Fig. 3b) was designed to fit inside the Anton Paar convection oven for parallel plate attachment, as depicted in Fig. 4a. Considering the DMA's maximum force limit of 40N, the mold diameter was determined to be 9.5 mm to reach pressure levels required for HPBC. In each experiment, 790 ± 31 milligrams of talc were loosely packed into the mold and covered with a plunger before being placed between the parallel plate attachment. To determine the talc behavior during the densification and compaction stage of HPBC the corresponding DMA tests were conducted:

- Compaction loading and unloading at constant strain rate of 30% per min and 10% per min, respectively.
    - Loosely packed talc (41% strain at 550 kPa)
    - Densified talc (7% strain at 550 kPa)

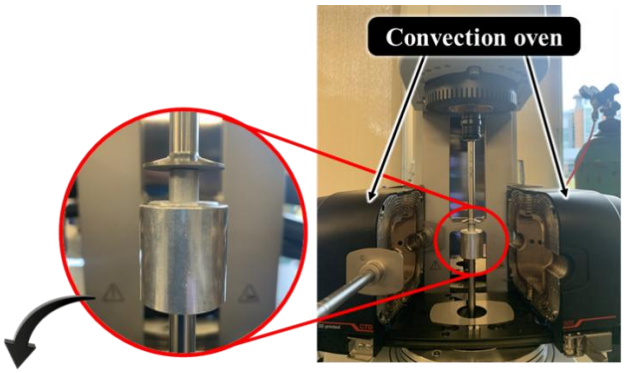

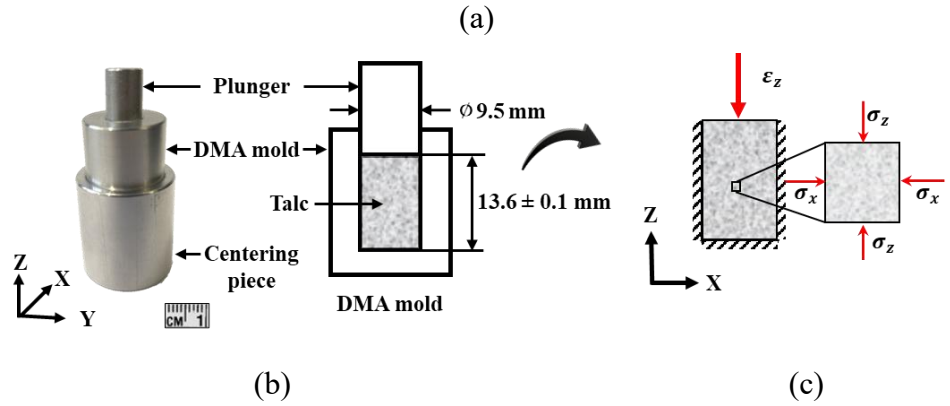

Figure 3: (a) DMA talc compaction test setup (b) 3-piece custom DMA closed-die design for uniaxial powder compaction and the volume of talc used for talc compaction (c) Boundary condition and stress element in talc under compaction.

The radial compaction (σ_{rad}) (shown in Fig. 3c) was also determined using the uniaxial unloading compaction test using Eq. 4. Based on the axial stress along with radial stress, hydrostatic stress (p) and von Mises equivalent stress (q) were then calculated as show in Eq. 4 and Eq. 5, respectively. The ratio of equivalent hydrostatic stress to von Mises stress was then used to determine the stress triaxiality factor (TF) during the uniaxial compression show in Eq. 6. The TF is used to evaluate the extent to which the stress state approaches true hydrostatic stress. A TF value of four or more [42] indicates a condition that closely represents true hydrostatic stress, providing a reliable parameter to determine the isostatic compaction on the MEX part using powder medium.

$$E(\rho_r) = \frac{\left(\frac{d\sigma_{ax}}{d\varepsilon_{ax}}\right)_{unloading} \cdot (1 + \nu(\rho_r))(1 - 2\nu(\rho_r))}{(1 - \nu(\rho_r))} \quad (1)$$

$$\frac{d\sigma_{ax}}{d\sigma_{rad}} = \frac{(1 - \nu(\rho_r))}{\nu(\rho_r)} \quad (2)$$

$$p = \frac{1}{3}(\sigma_{ax} + 2\sigma_{rad}) \quad (3)$$

$$q = |\sigma_{ax} - \sigma_{rad}| \quad (4)$$

$$TF = {}^{p}/_{q} \quad (5)$$

where σ_{ax} and σ_{rad} are axial and radial stress, respectively during the compaction test as shown in Fig. 4c.

DSC analysis

DSC analysis was performed on Shimadzu Corporation - DSC60A, to evaluate the crystallinity fraction and melting temperature range of both pristine and HBPC-treated specimens. DSC measures the heat flow required to change the temperature of a specimen relative to a standard reference sample. DSC allows to identify the temperatures of first and second-order transitions, such as the glass transition temperature and melting temperature range by capturing the exothermic and endothermic profiles during crystallization and melting processes, respectively. The HPBC-treated and as-printed specimens were placed under 50 mL/min of nitrogen atmosphere with a temperature ramp of 10°C/min, heated from 25°C to 260°C. The crystallinity fractions of the specimens were determined using the following equation during the heating cycle:

$$\chi_D = \frac{\Delta H_m}{C_m \Delta H_m^{100}} \tag{6}$$

where χ_D is crystallinity fraction, ΔH_m is crystalline melt enthalpy, C_m is the mass fraction of PA6 in SCF and ΔH_m^{100} fully crystallized PA6 melting enthalpy, 135 J/g [43]

Microscopy analysis

To examine inter- and intra-layer defects in the MEX printed specimen and the effect of HPBC on these imperfections, a microscopy analysis was performed. For sample preparation for microscopy, a longitudinal flexural specimen was sectioned using a ProtoMax waterjet and subsequently cured with quickset acrylic. The cured specimen was then subjected to a series of polishing steps. Initially, it was polished with P140 grit sandpaper, followed by P400 grit, and finally P600 grit, each step lasting 2-3 minutes with water as a lubricant. In the final polishing stage, 6-micron and 1-micron diamond paste, combined with a propylene glycol-based lubricant, was used, and this step continued for 10-15 minutes. These polishing steps were similarly applied to the two cross-sections of the rocker, which were cut using a water jet. All the polished cross-sectional images of the samples were then captured using a Leica DM6 M microscope at 10x magnification. The overall void fraction was calculated using ImageJ by analyzing two images for each specimen—pristine and HPBC. RGB thresholding was used to isolate the void region, and the void fraction was determined by measuring the ratio of voids to the total area in each image. The average void fraction for each specimen was obtained by averaging the results from both images.

Mechanical testing

To characterize the bending stiffness and flexural strength, a flexural test was performed in accordance with ASTM D790 on the five HPBC-treated and as-printed specimen. The test utilized a three-point bending setup, where the support rollers were placed 80 mm apart and the loading roller displaced at a rate of 2 mm/min. Flexural stress and strain stress were calculated through Eq. 9 and 10, respectively, where, applied load (L) and deflection (d) were obtained from the MTS machine for an 80 mm span length (S).

$$\sigma = \frac{3LS}{2bt^2} \quad (7) \qquad \varepsilon = \frac{6td}{S^2} \quad (8)$$

The five as-printed and HPBC-treated dogbone specimen based on ASTM D638 Type-I was tested using a 100 kN MTS machine, with one end fixed and the other end displaced at a rate of 1 mm/min. Force data was extracted from the MTS machine to calculate stress, while strain was captured using 3D GOM digital image correlation. Finally, the optimized rocker was tested under tensile load case-2 where BC_1 and BC_2 are fixed, and displacement of 2 mm/min was applied on push rod mount with MTS test machine (shown in Fig. 5b). A pre-load of 10 N was applied to eliminate any clearance from the tensile attachment.

4. Result and Analysis

This section presents the results of the study in three key areas: powder characterization, emphasizing the isostatic powder bed compaction process; coupon characterization, with a focus on enhanced interlaminar fusion; and a detailed analysis of the observed improvements in mechanical performance. Finally, it demonstrates the effective application of isostatic compaction on topologically complex shapes and translates the improved mechanical performance observed at the coupon level to the performance achieved in the HPBC-treated rocker.

Consolidation process analysis

The selected time-temperature-pressure parameters for HPBC have demonstrated superior consolidation performance compared to the limited interlayer consolidation observed in MEX-printed parts. The powder bed serves as a critical medium, facilitating isostatic compaction through a simplified mold setup. The methodology outlined in this study identifies key parameters that govern the successive application of isostatic pressure using a closed-die uniaxial compaction test. These tests have provided valuable data for quantifying hydrostatic stress and understanding stress relaxation during the densification and consolidation phases. To understand the powder's

mechanical behavior during the initial talc densification and MEX part densification stages, the stress-strain plot for loading and unloading from the uniaxial talc compaction test (Fig. 5b) was analyzed, with a maximum compaction pressure of 550 kPa (80 PSI). The elastic modulus of 188.4 MPa was calculated, with an estimated Poisson ratio of 0.392 [44] at a relative density of 48%. The radial stress (σ_{rad}) in the talc at the same relative density, was 72% axial compaction stress, resulting in hydrostatic stress of 447.3 kPa (65 PSI) and stress triaxiality factor of 2.96 on the MEX part inside the mold. The calculated stress triaxiality factor value, close to four — indicative of isostatic pressure [42]— provides a quantitative basis for the isostatic compaction achieved within the talc during the consolidation and densification stages.

Crystallinity and Polymorphism in PA6

The DSC data of thermoplastic laminate clearly displayed the emergence of a single peak near 215°C, revealing an endothermic transition associated with crystal melting. Notably, the melting peak for the HPBC specimen was observed at a higher temperature of 217°C in contrast to the pristine specimen, which exhibited a melting peak at 213°C. (as shown in Fig. 5). It is well-documented in the literature that PA6 exhibits crystallization behavior associated with two distinct crystal structures: the α-type and γ-type polymorphs [xx, xx]. The observed peak in the HPBC specimen indicates the presence of the α-type polymorph, identifiable by its higher melting temperature, whereas the γ-form exhibits a comparatively lower melting temperature [xx]. The higher melting temperature also suggests larger lamellae size, reflecting a more ordered and densely packed polymer structure, which in turn leads to increased crystallinity. The measured crystallinity fraction for the HPBC specimen was higher at 44.1% compared to the pristine prepreg sheet, which exhibited 31.51%.

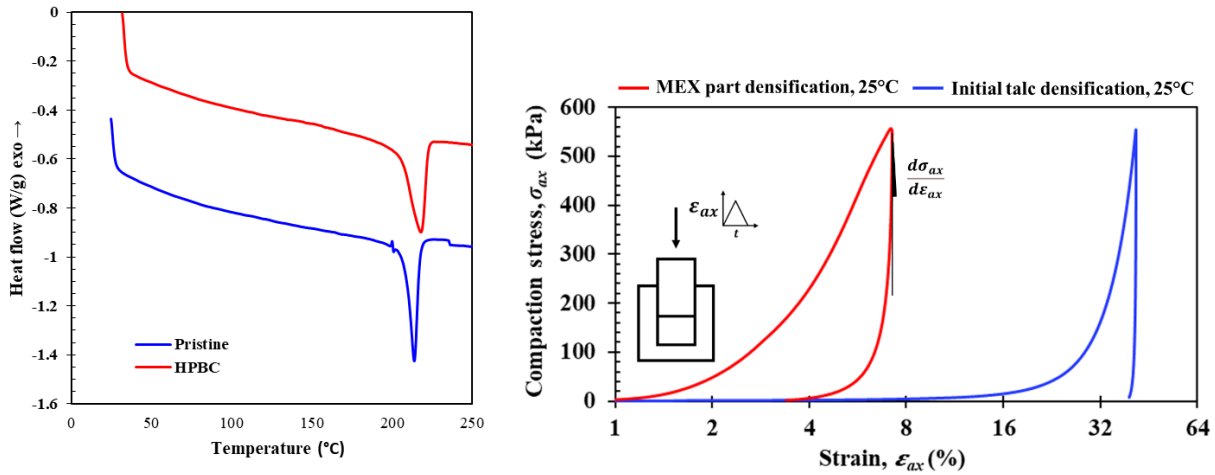

(a) (b)

Figure 4: DSC data comparison of HPBC specimen and pristine prepreg sheet (a) and Stress-strain plot for room temperature compaction test of loosely packed talc (densification stage) and densified talc (consolidation stage).

Morphological transformations in MEX composite after HPBC

As depicted in Fig. 8a, the micrograph reveals three types of voids in the MEX-printed sample: LCF-SCF inter-layer voids (V_{t1}), inter/intra SCF voids (V_{t2}), and LCF intralayer voids (V_{t3}). Additionally, a distinct separation line and cracks are evident between LCF and SCF in the pristine sample (as shown in Fig. 8a,c,e), resulting from partial inter-layer fusion during MEX layer-by-layer consolidation. The HPBC-treated samples, improved inter-layer fusion was achieved with LCF void closure (as shown in Fig. 8b,d.) and crack healing at the inter/intra region of SCF and LCF (as shown in Fig. 8f). Notably, some of the V_{t1} and V_{t3} type of voids are filled by the SCF, resulting in a void-free material system (as shown in Fig. 8d). This void infusion occurs at the consolidation stage, where the PA6 is fully melted, and due to the relatively lower viscosity of SCF compared to LCF viscosity and isostatic compaction, voids in LCF are filled with SCF.

Furthermore, the micrograph analysis was conducted on two cross-sections, *C1* and *C2*, of the pristine and HPBC-S2 rocker. The outline of cross-section *C1* demonstrated the HPBC process's capability to preserve complex geometries under powder bed isostatic compaction (shown in Fig. 8g). Additionally, another cross-section at *Pin-2* in the *C2* region revealed a notable reduction in voids and improved inter-layer fusion, as depicted in Fig. 8g. The synergy of void infusion, coupled with improved inter-layer fusion, has led to a reduced void and crack-free, fully consolidated microstructure with marginal shrinkage in the thickness/loading direction (Z-axis in

Fig. 1a). The thickness reduced by 18.45%, while width (Y-axis in Fig. 1a) increases by 11.89% for HPBC-treated tensile specimen, resulting 8.87 % reduction in area for weight reduction of 1.2%.

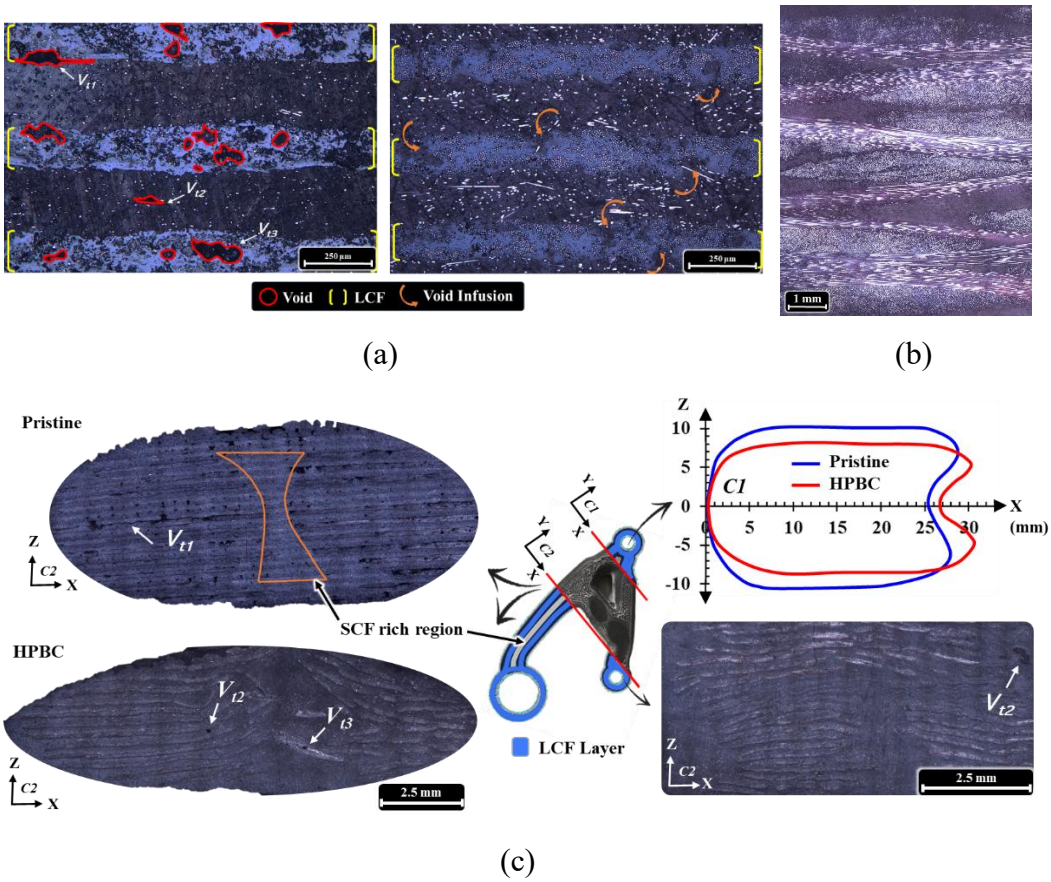

Figure 5: Micrograph of pristine and HPBC-treated coupon cross-section (a)with different types of voids and inter-layer cracks in pristine coupon; improved inter-layer fusion in HPBC-treated Glass fiber thermoplastic laminate (b). Microscopy analysis of different cross-sections of HPBC rocker (c).

Mechanical behavior and failure mechanism of MEX processed, HPBC-treated parts

The flexural test on the HPBC-treated longitudinal (0° LCF) specimens revealed a flexural modulus of 14.89 ± 0.59 GPa and a flexural strength of 360.66 ± 15.32 MPa (as depicted in Fig. 9a), marking a 30.16% and 36.38% increase, respectively, compared to the pristine specimens. Similarly, the HPBC-treated transverse (90° LCF) specimens exhibited a flexural modulus of 6.56 ± 0.09 GPa and a flexural strength of 145.87 ± 4.62 MPa (as shown in Fig. 9b), demonstrating a 74.47% and 63.99% increase, respectively, in comparison to the pristine specimens. However, the failure mode differed significantly, with the pristine failing with a ductile response, as shown in

Fig. 10a, whereas the treated coupon experienced a brittle fracture [31], clearly evident from Fig. 10b. This increase in modulus is the result of improved inter-layer fusion, void reduction and increases in strength is attributed improved fiber-matrix interface and reduced void fraction.

Under bending loads, the fracture initiated at the tension side, followed by LCF-SCF delamination (as shown in Fig. 11a) for pristine specimens. Further fracture analysis revealed fiber breakage and pullout, indicating a weak fiber-matrix interface in the pristine longitudinal flexural specimens (as shown in Fig. 11a-S3). In contrast, HPBC-treated specimens exhibited sharp fracture surfaces without fiber pullout, as shown in Fig. 11b-S1, signifying an improved fiber-matrix interface. The MEX-processed continuous fiber-reinforced thermoplastic resulted in rapid layer consolidation, which weakened the interface and led to premature failure, as shown by molecular dynamics simulations [45, 46] and scanning electron microscopy analysis [47] of fracture surface under different failure modes. Additionally, inter- and intra-layer micro-voids and cracks in pristine specimens hindered fiber-to-matrix stress transfer, causing stress concentrations and premature failure. HPBC treatment effectively healed micro-voids and cracks, enabling better stress transfer and enhancing fiber-matrix bonding.

In the case of the tensile testing, the modulus of longitudinal HPBC treated coupons showed 25.5±0.61 GPa elastic modulus and 285.66 ± 4.83 MPa tensile strength which is 21.7% and 65.9% superior compared to pristine specimen, as shown in Fig. 10c. In the transverse direction, the tensile modulus was increased by 36.8%, reaching 6.93 ± 0.22 GPa compared to the pristine specimen. Additionally, the tensile strength increases to 101.69 ± 1.43 MPa, marking a 57.24% improvement over the pristine specimen. Similar to the longitudinal bending specimens, the HPBC-treated tensile specimens showed no signs of fiber pullout indicating an improved fiber-matrix interface that enabled effective stress transfer between the fiber and matrix, ultimately resulting in higher mechanical performance.

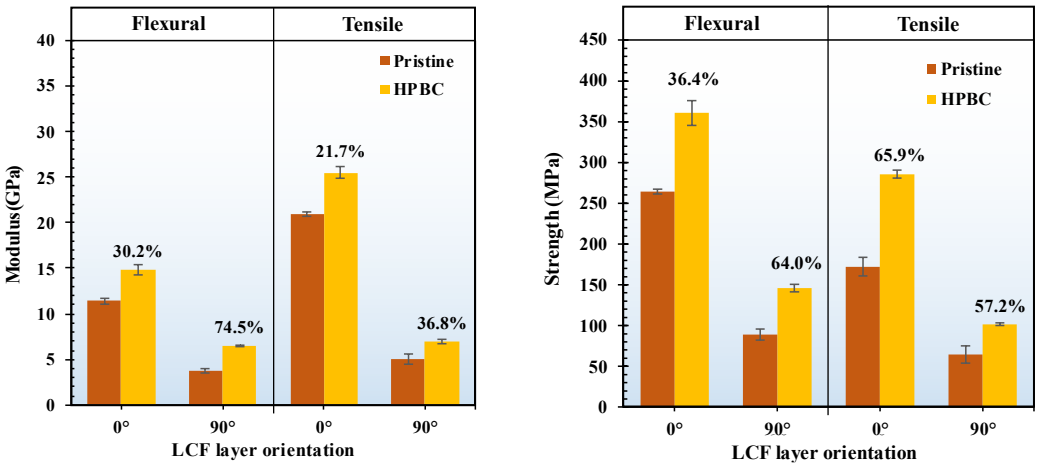

(a) *(b)*

Figure 6: Summary of mechanical testing for MEX processed pristine and HPBC-treated specimens. (a) Modulus and (b) strength for longitudinal (0°) and traverse (90°) specimens

In summary, the HPBC-treated specimens exhibited improved interlaminar fusion and a strengthened fiber-matrix interface, along with reduced void fraction, as evidenced by enhanced flexural and tensile properties in both directions. The shift in failure behavior was attributed to material reconsolidation, which reduced energy dissipation in inter-layer delamination and altered the PA6 phase [30, 48], leading to a more brittle response. A summary of the improvements in modulus and strength for both tensile and flexural tests is shown in Fig. 11.

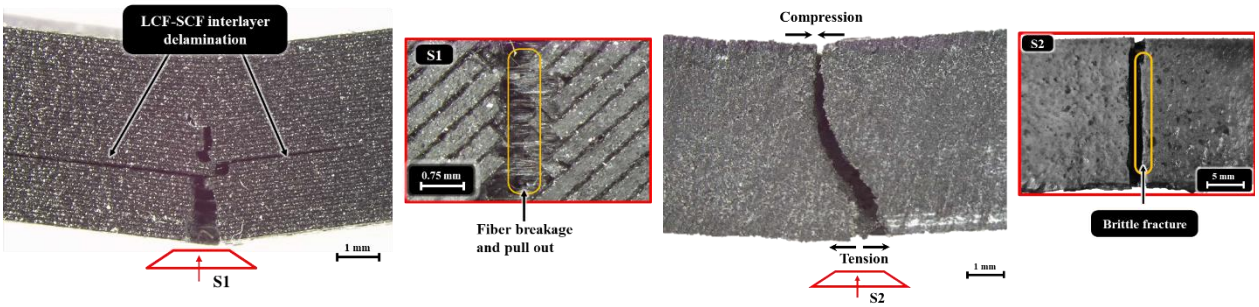

(a) *(b)*

Figure 7 : Micrograph analysis of (a) longitudinal pristine specimen and (b) HPBC-treated longitudinal specimens under bending.

The tensile test conducted on the HPBC-treated rocker, illustrated in the force-

displacement plot (Fig. 8a), revealed a stiffness of 2.25 kN/mm and a failure strength of 4.64 kN, indicating an increase of 31.3% and 4%, respectively for S2 LCF layer configuration, compared to the pristine rocker. And for S1 LCF layer configuration 32.8% and 24.3% increases in stiffness and strength was observed. Both pristine and HPBC-treated rockers, shown in Fig. 12b and 12c, failed at the push rod mount.

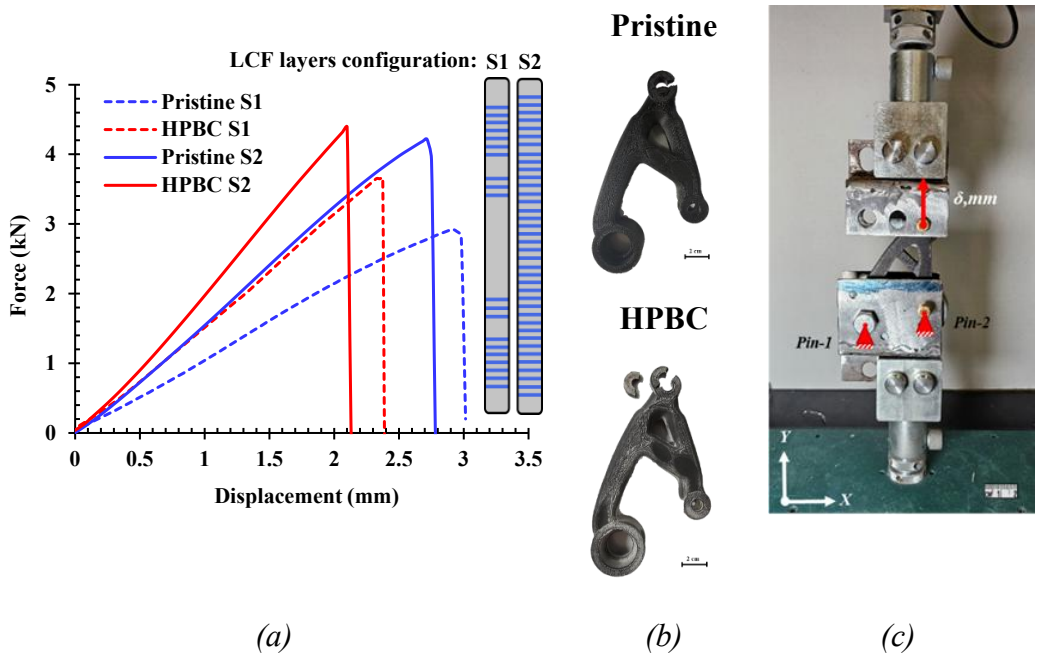

(a) *(b)* *(c)*

Figure 8: (a) Force-displacement plot for pristine and HPBC-treated under tensile for load case 2, (b) pristine rocket failure, and HPBC rocket failure at push rod mount. (c) The rocker tensile test setup under load case-2

The flexural performance of the HPBC-treated R4 and R2 sandwich beams showed a significant improvement compared to their pristine counterparts. The HPBC-treated structure exhibited a stiffness per unit width of 231 ± 4.1 N/mm², compared to the pristine, which measured 107.6 ± 4.4 N/mm²—a 2.16 times increase. In terms of peak strength, the treated sample achieved 753.0 ± 30.2 N/mm, corresponding to a 2.46 times enhancement over the untreated part. Alongside these mechanical enhancements, distinct differences in failure behavior and damage progression were observed. The pristine sandwich structures, characterized by a ductile PA6 matrix, began yielding at around 210 N/mm, with localized compression in the top truss region under the loading roller. Final failure occurred when the bottom skin fibers fractured under tension. In contrast, the HPBC-treated samples exhibited a transition in PA6 phase behavior from ductile to brittle and improved fiber-matrix stress transfer, fundamentally altered

the structural failure progression. The R4 core in these samples yielded at a higher load of 640 N/mm. Cracking initiated on the tension side and propagated rapidly through the core, to the top skin and splits into two pieces. These results clearly demonstrate the effectiveness of HPBC's bulk consolidation method to improve performance by preserves the detailed sandwich core features.

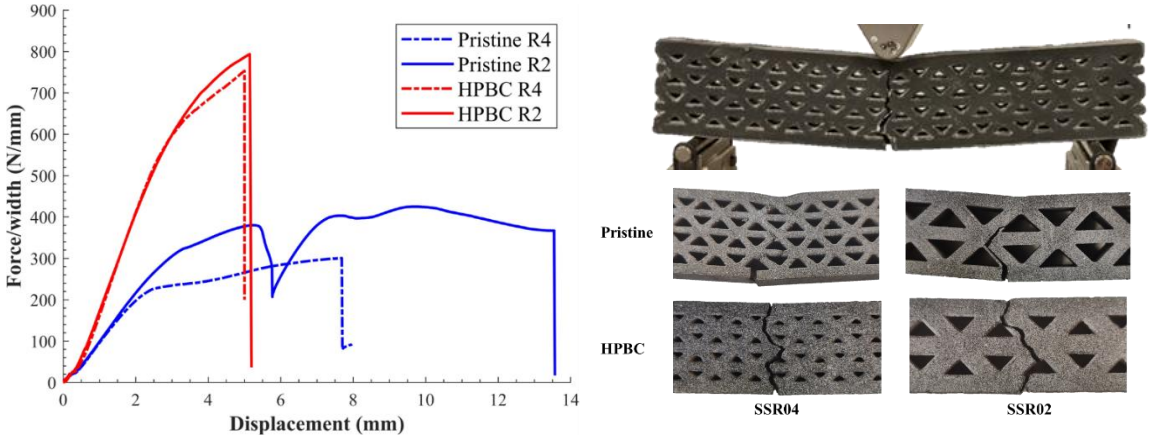

Figure 9: Three point bending results of pristine and HPBC treated of sandwich structure.

5. Conclusions

This study evaluated the mechanics of the HPBC process in achieving isostatic compaction and its impact on MEX-processed parts composed of complex-shaped, multi-fiber morphology material systems with a semi-crystalline PA6 matrix. A topological component with short and long carbon fibers was used to demonstrate the capabilities of HPBC process. The HPBC process demonstrated as a three-step bulk-consolidation technique utilizing a powder medium, involves densification, bulk heating until the matrix reaches the molten stage, and consolidation under isostatic compaction with room-temperature cooling. The densification stage of the powder was shown to be critical in supporting multi-fiber morphology material systems during the molten stage.

The powder medium used in the HPBC process demonstrated effective application of hydrostatic pressure of 65 PSI during consolidation with stress triaxiality factor 2.96, as demonstrated by close-die uniaxial powder compaction experiment. This consolidation compaction pressure allowed to eliminate MEX defects, as demonstrated by microscopic analysis. Bending and tensile tests demonstrated significantly enhanced mechanical performance, attributed to crack healing, improved interlayer fusion, and a strengthened fiber-matrix interface. The

fracture behavior transitioned from delamination, ductile matrix failure, fiber breakage, and pullout to brittle matrix failure, characterized by sharp fracture surfaces with no evidence of fiber pullout or delamination. Notably, tensile testing of the HPBC-treated topological rockers showed a 31.3% increase in stiffness, attributed to the effective bulk-consolidation. In the case of R4/R2 sandwich structures, HPBC further preserved the unit cell shape and core dimensions while improving fiber–matrix stress transfer as demonstrated from improved flexural performance. This led to effective load transmission between the skin and core, resulting in more than 216% and 246% increases in both stiffness and strength, respectively.

The study utilized a basic HPBC setup, separating the compaction stage and heating stage. A more advanced setup with a heated mold and cooling channels inside of the generalized box configuration can improve processing parameters that affect polymer crystallinity [49], [50] and thus mechanical properties. In summary, the HPBC allows to achieve superior mechanical properties when combined with the traditional MEX process. HPBC's flexible fusion approach allows to reach needed consolidation under isostatic conditions without relying on the use of rigid tooling. Therefore, this technique can enable the creation of topological structures for which no rigid tool can be implemented.

6. Reference

[1] Bhattacharyya, D.: Composite Sheet Forming, accessed 10 November 2023.
[2] Chen, H.; Li, S.; Wang, J. and Ding, A.: A focused review on the thermo-stamping process and simulation progresses of continuous fibre reinforced thermoplastic composites, Composites Part B: Engineering, **224** (2021), p. 109196.
[3] Mallick, P.K.: Thermoplastics and thermoplastic–matrix composites for lightweight automotive structures, Materials, Design and Manufacturing for Lightweight Vehicles (Second Edition), Woodhead Publishing, 2021, pp. 187–228.
[4] Martín, I.; Fernández, K.; Cuenca, J.; Sánchez, C.; Anaya, S. and Élices, R.: Design and manufacture of a reinforced fuselage structure through automatic laying-up and in-situ consolidation with co-consolidation of skin and stringers using thermoplastic composite materials, Heliyon, **9** (2023), no. 1, p. e12728.
[5] Bhagatji, J.: Development, Experimental Validation, and Progressive Failure Modeling of an Ultra-Thin High Stiffness Deployable Composite Boom for in-Space Applications, Mechanical & Aerospace Engineering Theses & Dissertations, (2023).
[6] Vieille, B.; Casado, V.M. and Bouvet, C.: About the impact behavior of woven-ply carbon fiber-reinforced thermoplastic- and thermosetting-composites: A comparative study, Composite Structures, **101** (2013), pp. 9–21.
[7] Vieille, B.; Casado, V.M. and Bouvet, C.: Influence of matrix toughness and ductility on the compression-after-impact behavior of woven-ply thermoplastic- and thermosetting-composites: A comparative study, Composite Structures, **110** (2014), pp. 207–218.

[8] Erland, S.; Stevens, H. and Savage, L.: The re-manufacture and repairability of poly(ether ether ketone) discontinuous carbon fibre composites, Polymer International, **70** (2021), no. 8, pp. 1118–1127.
[9] Mohammad, S.: Restoration of Strength in Polyamide Woven Glass Fiber Organosheet by Hot-Pressing: Case Study of Impact and Compression after Impact, Polymers, (2024).
[10] Bernatas, R.; Dagreou, S.; Despax-Ferreres, A. and Barasinski, A.: Recycling of fiber reinforced composites with a focus on thermoplastic composites, Cleaner Engineering and Technology, **5** (2021), p. 100272.
[11] Schmidt, M.-P.; Couret, L.; Gout, C. and Pedersen, C.B.W.: Structural topology optimization with smoothly varying fiber orientations, Structural and Multidisciplinary Optimization, **62** (2020), no. 6, pp. 3105–3126.
[12] Liu, T.; Yuan, S.; Wang, Y.; Xiong, Y.; Zhu, J.; Lu, L. and Tang, Y.: Stress-driven infill mapping for 3D-printed continuous fiber composite with tunable infill density and morphology, Additive Manufacturing, **62** (2023), p. 103374.
[13] Rejab, M.R.M. and Cantwell, W.J.: The mechanical behaviour of corrugated-core sandwich panels, Composites Part B: Engineering, **47** (2013), pp. 267–277.
[14] Lok, T.-S. and Cheng, Q.-H.: Elastic Stiffness Properties and Behavior of Truss-Core Sandwich Panel, Journal of Structural Engineering, **126** (2000), no. 5, pp. 552–559.
[15] Wicks, N. and Hutchinson, J.W.: Performance of sandwich plates with truss cores, Mechanics of Materials, **36** (2004), no. 8, pp. 739–751.
[16] Hsieh, T.-H.; Chang, T.-Y.; Guo, B.-W. and Tsai, S.-N.: Mechanical properties of sandwich panels with corrugated carbon fiber cores, Journal of Composite Materials, **58** (2024), no. 20, pp. 2231–2245.
[17] Ullah, I.; Elambasseril, J.; Brandt, M. and Feih, S.: Performance of bio-inspired Kagome truss core structures under compression and shear loading, Composite Structures, **118** (2014), pp. 294–302.
[18] Côté, F.; Deshpande, V.S.; Fleck, N.A. and Evans, A.G.: The compressive and shear responses of corrugated and diamond lattice materials, International Journal of Solids and Structures, **43** (2006), no. 20, pp. 6220–6242.
[19] Experimental and Analytical Characterization of Fluted-Core Sandwich Composite Structures - NASA Technical Reports Server (NTRS), https://ntrs.nasa.gov/citations/20210000643, accessed 21 April 2025.
[20] Yang, H.; Zhang, H.; Li, X.; Yin, L.; Guo, X.; Fan, H. and Lei, H.: Load-bearing capacity and failure mechanism of integrated fluted-core composite sandwich cylinders, Composites Science and Technology, **221** (2022), p. 109344.
[21] Zhou, J.; Guan, Z.W. and Cantwell, W.J.: Scaling effects in the mechanical response of sandwich structures based on corrugated composite cores, Composites Part B: Engineering, **93** (2016), pp. 88–96.
[22] Hassan, A.; Yahya, R.; Yahaya, A.H.; Tahir, A.R.M. and Hornsby, P.R.: Tensile, Impact and Fiber Length Properties of Injection-Molded Short and Long Glass Fiber-Reinforced Polyamide 6,6 Composites, Journal of Reinforced Plastics and Composites, **23** (2004), no. 9, pp. 969–986.
[23] Crowson, R.J.; Folkes, M.J. and Bright, P.F.: Rheology of short glass fiber-reinforced thermoplastics and its application to injection molding I. Fiber motion and viscosity measurement, Polymer Engineering & Science, **20** (1980), no. 14, pp. 925–933.
[24] Sattar, S.; Beltran Laredo, B.; Pedrazzoli, D.; Zhang, M.; Kravchenko, S.G. and Kravchenko, O.G.: Mechanical behavior of long discontinuous glass fiber nylon composite produced by in-situ polymerization, Composites Part A: Applied Science and Manufacturing, **154** (2022), p. 106779.
[25] Aliyeva, N.; Sas, H.S. and Saner Okan, B.: Recent developments on the overmolding process for the fabrication of thermoset and thermoplastic composites by the integration of nano/micron-scale reinforcements, Composites Part A: Applied Science and Manufacturing, **149** (2021), p. 106525.

[26] Akkerman, R.; Bouwman, M. and Wijskamp, S.: Analysis of the Thermoplastic Composite Overmolding Process: Interface Strength, Frontiers in Materials, **7** (2020).
[27] Subramaniyan, S.K.: Manufacture and Testing Carbon Fibre Lattice Core Sandwich Structures2019.
[28] Chacón, J.M.; Caminero, M.A.; Núñez, P.J.; García-Plaza, E.; García-Moreno, I. and Reverte, J.M.: Additive manufacturing of continuous fibre reinforced thermoplastic composites using fused deposition modelling: Effect of process parameters on mechanical properties, Composites Science and Technology, **181** (2019), p. 107688.
[29] Parlevliet, P.P.; Bersee, H.E.N. and Beukers, A.: Residual stresses in thermoplastic composites—A study of the literature—Part I: Formation of residual stresses, Composites Part A: Applied Science and Manufacturing, **37** (2006), no. 11, pp. 1847–1857.
[30] Barber, J.; Revolinsky, P.; Spinelli, E.; Jamora, V.C.; Eisazadeh, H. and Kravchenko, O.G.: Investigation of high temperature compaction on fracture toughness of 3D printed carbon fiber polyamide composites, Progress in Additive Manufacturing, (2023).
[31] Polymorphism and Mechanical Behavior in Hot Pressed 3d Printed Polyamide Composite: Effects of Pressure and Temperature by John Barber, P. Revolinsky, J. Bhagatji, D. Pedrazzoli, S. G. Kravchenko, Oleksandr G. Kravchenko :: SSRN, https://papers.ssrn.com/sol3/papers.cfm?abstract_id=4748835, accessed 14 May 2024.
[32] Kumar Jain, P.A.; Sattar, S.; Mulqueen, D.; Pedrazzoli, D.; Kravchenko, S.G. and Kravchenko, O.G.: Role of annealing and isostatic compaction on mechanical properties of 3D printed short glass fiber nylon composites, Additive Manufacturing, **51** (2022), p. 102599.
[33] Bhagatji, J. and Kravchenko, O.: Hot Powder Bed Compaction: A Rapid Fabrication Approach for Thermoplastic Composite Components - ScienceDirect, accessed 14 May 2024.
[34] Bocanegra-Bernal, M.H.: Hot Isostatic Pressing (HIP) technology and its applications to metals and ceramics, Journal of Materials Science, **39** (2004), no. 21, pp. 6399–6420.
[35] Loh, N.L. and Sia, K.Y.: An overview of hot isostatic pressing, Journal of Materials Processing Technology, **30** (1992), no. 1, pp. 45–65.
[36] van de Werken, N.; Koirala, P.; Ghorbani, J.; Doyle, D. and Tehrani, M.: Investigating the hot isostatic pressing of an additively manufactured continuous carbon fiber reinforced PEEK composite, Additive Manufacturing, **37** (2021), p. 101634.
[37] Onyx, https://markforged.com/materials/plastics/onyx, accessed 18 November 2023.
[38] Kabir, S.M.F.; Mathur, K. and Seyam, A.-F.M.: The Road to Improved Fiber-Reinforced 3D Printing Technology, Technologies, **8** (2020), no. 4, p. 51.
[39] Fasco Talc Powder, Fasco Epoxies, Inc., https://fascoepoxies.com/Fasco-Talc-Powder.html, accessed 14 January 2025.
[40] Altair Student Edition, https://web.altair.com/altair-student-edition, accessed 3 June 2024.
[41] Modular Compact Rheometer: MCR 702e, Anton Paar, https://www.anton-paar.com/us-en/products/details/rheometer-mcr-702-multidrive/, accessed 14 January 2025.
[42] Melo, C.C.; Moraes, A.L.I.; Rocco, F.O.; Montilha, F.S. and Canto, R.B.: A validation procedure for numerical models of ceramic powder pressing, Journal of the European Ceramic Society, **38** (2018), no. 8, pp. 2928–2936.
[43] Sattar, S.; Pedrazzoli, D.; Zhang, M.; Kravchenko, S.G. and Kravchenko, O.G.: Notched tensile strength of long discontinuous glass fiber reinforced nylon composite, Composites Part A: Applied Science and Manufacturing, **163** (2022), p. 107217.
[44] Diarra, H.; Mazel, V.; Boillon, A.; Rehault, L.; Busignies, V.; Bureau, S. and Tchoreloff, P.: Finite Element Method (FEM) modeling of the powder compaction of cosmetic products: Comparison between simulated and experimental results, Powder Technology, **224** (2012), pp. 233–240.

[45] Kong, X.; Luo, J.; Luo, Q.; Li, Q. and Sun, G.: Experimental study on interface failure behavior of 3D printed continuous fiber reinforced composites, Additive Manufacturing, **59** (2022), p. 103077.
[46] Atomistic Modeling of the Effect of Temperature on Interfacial Properties of 3D-Printed Continuous Carbon Fiber-Reinforced Polyamide 6 Composite: From Processing to Loading | ACS Applied Materials & Interfaces, https://pubs.acs.org/doi/10.1021/acsami.3c12372, accessed 13 January 2025.
[47] He, Q.; Wang, H.; Fu, K. and Ye, L.: 3D printed continuous CF/PA6 composites: Effect of microscopic voids on mechanical performance, Composites Science and Technology, **191** (2020), p. 108077.
[48] Maqsood, N. and Rimašauskas, M.: Delamination observation occurred during the flexural bending in additively manufactured PLA-short carbon fiber filament reinforced with continuous carbon fiber composite, Results in Engineering, **11** (2021), p. 100246.
[49] Nasr, A. and Svoboda, P.: Influence of Fusion Temperature on Nonisothermal Crystallization Kinetics of Polyamide 6, Polymers, **15** (2023), no. 8, p. 1952.
[50] Wu, B.; Gong, Y. and Yang, G.: Non-isothermal crystallization of polyamide 6 matrix in all-polyamide composites: crystallization kinetic, melting behavior, and crystal morphology, Journal of Materials Science, **46** (2011), no. 15, pp. 5184–5191.